

Graph-Loc: Robust Graph-Based LiDAR Pose Tracking with Compact Structural Map Priors under Low Observability and Occlusion

Wentao Zhao, Yihe Niu, Zikun Chen, Rui Li, Yanbo Wang, Tianchen Deng,
Jingchuan Wang*, *Senior Member, IEEE*

Abstract—Map-based LiDAR pose tracking is essential for long-term autonomous operation, where onboard map priors need be compact for scalable storage and fast retrieval, while online observations are often partial, repetitive, and heavily occluded. We propose Graph-Loc, a graph-based localization framework that tracks the platform pose against compact structural map priors represented as a lightweight point-line graph. Such priors can be constructed from heterogeneous sources commonly available in practice, including polygon outlines vectorized from occupancy/grid maps and CAD/model/floor-plan layouts. For each incoming LiDAR scan, Graph-Loc extracts sparse point and line primitives to form an observation graph, retrieves a pose-conditioned visible subgraph via LiDAR ray simulation, and performs scan-to-map association through unbalanced optimal transport with a local graph-context regularizer. The unbalanced formulation relaxes mass conservation, improving robustness to missing, spurious, and fragmented structures under occlusion. To enhance stability in low-observability segments, we estimate information anisotropy from the refinement normal matrix and defer updates along weakly constrained directions until sufficient constraints reappear. Experiments on public benchmarks, controlled stress tests, and real-world deployments demonstrate accurate and stable tracking with KB-level priors from heterogeneous map sources, including under geometrically degenerate and sustained occlusion and in the presence of gradual scene changes.

Note to Practitioners—Long-term deployment of LiDAR-based localization often requires storing a prior map onboard with strict memory and retrieval constraints, while the robot operates in environments with repetitive structure, partial visibility, and frequent occlusions. Graph-Loc addresses this setting by using a compact structural map representation (a lightweight point-line graph) that can be built from commonly available sources such as occupancy/grid-map outlines and CAD or floor-plan layouts. In operation, the method retrieves only the locally visible portion of the map for matching, which reduces computation and supports fast updates. This design is particularly useful in structured environments (e.g., buildings, corridors, and industrial sites), where geometric observability may temporarily degrade or be blocked by dynamic obstacles. The system outputs incremental platform pose updates and is intended as a drop-in module for navigation stacks that require stable tracking under limited onboard resources.

Index Terms—LiDAR localization, compact map prior, optimal transport, occlusion robustness

Wentao Zhao, Zikun Chen, Yanbo Wang, Tianchen Deng, and Jingchuan Wang are with the School of Automation and Intelligent Sensing, Institute of Medical Robotics, Shanghai Jiao Tong University, Shanghai 200240, China. Yihe Niu is with the School of Mathematical Sciences Shanghai Jiao Tong University. Rui Li is with Shenzhen Qingmang Robotics Technology Co., Ltd. Jingchuan Wang (jchwang@sjtu.edu.cn) is the corresponding authors.

I. INTRODUCTION

Reliable LiDAR localization against an onboard map (map-based pose tracking) is a core capability for intelligent vehicles and mobile robots operating over long time horizons. In practical deployments, two requirements often conflict: the onboard map must be compact for scalable storage and fast retrieval, yet sufficiently discriminative to support robust data association in the presence of real-world clutter and occlusion [1], [2]. Dense point-cloud maps preserve rich geometry but quickly become expensive to store and query as the covered area grows [3]–[5]. This has motivated structural map representations that encode lightweight geometric elements, including polygonal maps [6], [7], which represent free space and boundaries as compact polygons, as well as road boundaries, curbs, and layout skeletons; such representations are widely adopted in automation and mapping pipelines [8]. However, reliable localization with compact structural maps remains challenging when the environment is repetitive, only partially visible, and frequently occluded by surrounding agents [9].

A central challenge is that data association becomes fragile when the scene provides weak geometric constraints. In man-made infrastructures such as parking garages, campuses, depots, and corridors, large portions of a trajectory may be dominated by low-distinctiveness structures, including long straight boundaries and repeated parallel walls [10]. Such geometrically degenerate configurations reduce observability and make greedy correspondence search brittle: incorrect matches can appear plausible, persist over time, and induce substantial drift. A common remedy in compact-outline-based localization is to split long or irregular primitives into shorter segments to increase matchability [6]. While helpful in some cases, splitting inflates the map representation and increases offline processing complexity, and it still struggles when ambiguity is intrinsic due to repetitive layouts and partial observations. In this work, we assume a fixed compact map available onboard (from offline mapping or existing layouts) and focus on robust scan-to-map pose tracking, without requiring high-level semantic annotations or online map updating.

We address these issues by strengthening the association through graph-level structural matching, rather than increasing feature density. The onboard map is represented as a lightweight point-line graph, and each incoming scan is converted into an observation graph using sparse structural point and line features extracted from range discontinuities

and local geometric consistency. Nodes encode geometric features and proximity edges capture local context, turning scan-to-map localization into a graph matching problem where correspondences should be consistent not only per feature but also in their neighborhood relations. This abstraction also accommodates heterogeneous priors commonly available in practice, ranging from polygon outlines vectorized from occupancy/grid-style maps to model/CAD/floor-plan layout priors when accessible.

To compute robust correspondences, we formulate scan-to-map matching as unbalanced optimal transport over graph nodes with a graph-context regularizer. Unlike nearest-neighbor pipelines that commit to local decisions early [3], [6], [11], optimal transport estimates a globally consistent transport plan whose assignments are coupled across all nodes. The unbalanced formulation relaxes strict mass conservation, making the association tolerant to missing structures, spurious returns, and feature fragmentation caused by occlusions and sensing artifacts.

Even with robust matching, low-observability segments can still yield ill-conditioned pose updates. We therefore introduce a degeneracy-aware delayed optimization strategy: weakly constrained motion directions are detected from information anisotropy, their updates are temporarily deferred while evidence accumulates, and a full update is released once constraints recover. This stabilizes tracking in structurally degenerate segments and prevents transient association noise from dominating the estimate.

We evaluate our method on large-scale public benchmarks, controlled indoor tests, and real-world deployments. Experiments on KITTI [12] and the ERPoT dataset [6] assess scalability and the accuracy-compactness trade-off in large outdoor scenes. A controlled simulation based on CMU-EXPLORATION [13] stresses degeneracy under systematically increasing pedestrian occlusions, while real-world experiments further evaluate robustness under sustained interference and long-range tracking in an outdoor parking-lot environment, where structural change (e.g., parked vehicles and temporary obstacles) introduces mismatches between online observations and a fixed map.

Our main contributions are:

- A compact structural localization framework that represents maps and observations as lightweight point-line graphs, supporting heterogeneous compact map sources (occupancy/grid outlines and, when available, CAD/model/floor-plan layouts).
- An unbalanced optimal transport formulation with graph-context regularization for robust scan-to-map association under missing, spurious, and ambiguous structures.
- A degeneracy-aware delayed optimization strategy that stabilizes pose updates in low-observability segments.
- Extensive evaluation on public benchmarks, controlled simulation, and real deployments, demonstrating competitive accuracy with consistently compact maps under occlusion and gradual structural change.

II. RELATED WORK

Our work targets practical compact priors for LiDAR localization and studies how to maintain reliable association and stable estimation when observations are weakly informative. We review related work from three aspects: compact structural priors, data association and robust matching, and degeneracy-aware optimization.

A. Compact Structural Priors

Most practical LiDAR localization systems adopt dense point-cloud priors as onboard maps (e.g., LOAM-style pipelines such as ALOAM [3] and FLOAM [5]), KISS_MCL [4], and HDL_LOC [14]. To reduce memory footprint and support scalable storage and fast retrieval, dense point-cloud priors are often compacted via strategies such as submapping and keyframe selection [15], [16]. Dense point-cloud priors can also be compacted via alternative map abstractions, e.g., voxel/implicit encodings [17] or mesh-based representations [18].

Beyond geometric compression, structural priors exploit man-made regularities to produce compact and interpretable abstractions, including CAD/architectural layouts [11], [19], floor-plan assisted localization [20], [21], and wall/outline extraction via segmentation or layout parsing [22]. Another practical and widely used class is polygonal/outline maps, which derive structure from occupancy/grid-style maps by vectorizing obstacles and boundaries into polylines or polygons. Representative systems such as ERPoT [6] localize against polygon outlines distilled from offline occupancy maps, achieving strong compactness and fast retrieval. However, compactness alone does not guarantee reliable tracking: in low-distinctiveness or partially observed scenes, long boundaries and repeated structures yield many locally plausible matches, making association fragile. To improve matchability, some outline-based pipelines split long or irregular contours into shorter segments, effectively increasing map density at the cost of additional offline processing and map inflation. In contrast, our work targets the same practicality of compact structural priors but avoids relying on contour splitting by strengthening association through a relational graph abstraction and global matching.

B. Data Association and Robust Matching

Data association is a key bottleneck for map-based localization, especially when observations are weakly informative due to repetition and occlusions, which frequently occur in real-world deployments [1]. ICP and its variants [23], [24] and NDT-style methods [25], [26] are widely used for scan-to-map registration, but they can degrade under partial overlap, clutter, or dynamics, where nearest-neighbor hard correspondences become brittle. Feature-based pipelines improve efficiency by extracting salient geometric cues; LOAM [3] is a milestone that uses edge and planar features for registration, and many subsequent systems adopt similar front-ends for odometry and mapping.

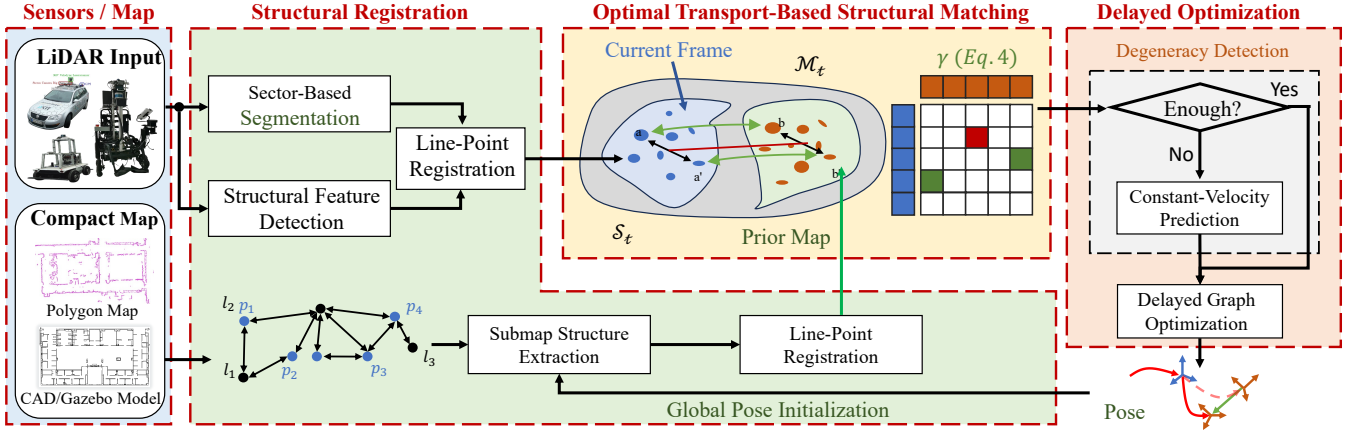


Fig. 1: System overview of Graph-Loc. Each LiDAR scan is converted into structural point/line features and organized as an observation graph. A pose-conditioned visible subgraph is retrieved from a compact prior (polygon outlines or CAD/model layouts). Scan-to-map association is solved by unbalanced optimal transport to obtain globally consistent soft correspondences, followed by a degeneracy-aware delayed update for stable real-time pose tracking under occlusion and low observability.

Several practical localization systems build global pose tracking on top of such association mechanisms. LOAM-style pipelines (e.g., ALOAM [3] and FLOAM [5]) typically rely on feature-level correspondences and iterative alignment. KISS_MCL [4] follows an ICP-based registration philosophy designed for robustness with minimal tuning, while HDL_LOC [14] represents a widely used scan-matching localization stack that combines scan-to-map alignment with filtering. Despite their effectiveness, these pipelines largely depend on hard or locally-coupled correspondence decisions, which can be ambiguous when many matches are locally plausible in repetitive structures or when observations are heavily occluded.

For compact structural priors, however, many pipelines still depend on local correspondence search with hard assignments and heuristic consistency checks. When the map prior contains repeated or elongated structures and the scan is only partially visible, local matching produces many plausible candidates and can lock onto incorrect correspondences. This limitation is also reflected in outline-based tracking systems such as ERPoT [6], where association is primarily driven by local geometric consistency and can become ambiguous under repetition and partial visibility. Optimal transport offers an alternative by estimating a global soft assignment between two sets of entities; entropic regularization enables efficient computation [27], and unbalanced formulations relax mass conservation to tolerate missing and spurious elements under occlusion. PS_LOC [28] follows this direction by applying optimal-transport-based matching between structural features, improving robustness over greedy local association when outliers and missing features are present. Building on this line, our method formulates scan-to-map association as unbalanced optimal transport on graph nodes with a graph-context regularizer, so correspondences are selected jointly under neighborhood consistency rather than by independent nearest-neighbor decisions, improving robustness without inflating the map prior.

C. Degeneracy Handling and Optimization

Even with improved association, weakly informative observations can lead to ill-conditioned estimation, where available constraints weakly determine certain motion directions. Prior work improves stability by incorporating structural regularities such as parallelism and orthogonality [29]–[31], by jointly modeling and associating multiple structural primitives [28], or by using relational/graph abstractions to provide additional context [32]–[34]. Nevertheless, degeneracy can still arise when observations concentrate in a few dominant directions (e.g., long straight boundaries), which is common in corridors, garages, and parking-lot traversals.

This motivates strategies that explicitly detect weak observability and stabilize updates, for example through adaptive regularization or delayed refinement when constraints are insufficient. Our work follows this direction but targets a more explicit directional treatment: weakly constrained motion directions are detected online and temporarily withheld while evidence accumulates, and a full update is released once observability recovers. This delayed strategy complements robust optimal-transport-based association and improves reliability under low-informativeness observations.

III. METHOD

A. Problem Statement and Framework

Figure 1 overviews the proposed pipeline for map-based LiDAR pose tracking with a fixed prior map. We consider ground-vehicle and indoor ground-navigation scenarios (e.g., roads, parking lots, and indoor floors), where the dominant motion is planar. Accordingly, we perform 3-DoF tracking in the horizontal plane and parameterize the pose by planar translation and yaw:

$$\mathbf{p}_t = [x_t, y_t, \phi_t]^\top, \quad \mathbf{P}_t \in \text{SE}(2). \quad (1)$$

The LiDAR scan at time t is denoted by \mathbf{X}_t . Our goal is to estimate the global pose \mathbf{P}_t of each scan with respect to the

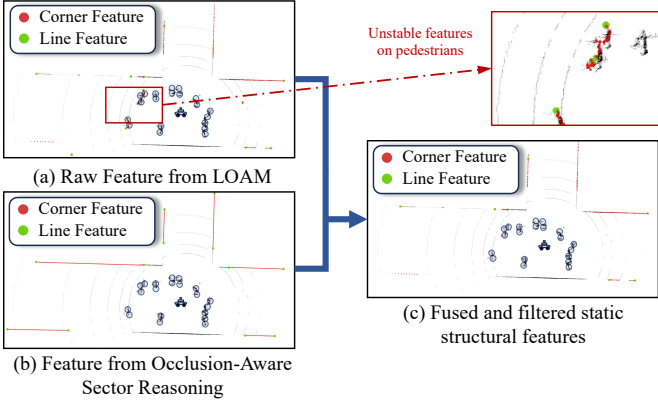


Fig. 2: Qualitative results of feature extraction and fusion on high-occlusion environments. (a) LOAM-style short features. (b) Sector-based structural long features. (c) Fused and filtered features used to build \mathcal{S}_t .

prior map while maintaining reliable scan-to-map association under partial visibility and occlusion.

Starting from a LiDAR front end, each scan is converted into sparse structural measurements. Specifically, we extract geometric cues from range discontinuities and local surface consistency, and consolidate them into two feature types: point features and line features. These sparse features provide an efficient abstraction while retaining stable geometric evidence for association.

To incorporate local context without sacrificing compactness, both observations and the prior map are represented as graphs (Sec. III-B). For the current scan, we construct an observation graph $\mathcal{S}_t = (\mathcal{V}_t, \mathcal{E}_t)$, where each node $v \in \mathcal{V}_t$ corresponds to a point or line feature with geometric attributes (e.g., position and orientation). Edges \mathcal{E}_t encode local neighborhood structure via Euclidean k -nearest neighbors based on representative positions (point locations and line anchors). Likewise, the offline prior map is represented as a fixed graph $\mathcal{M} = (\mathcal{V}^M, \mathcal{E}^M)$.

Given a pose prediction $\hat{\mathbf{P}}_t$ computed from the previous estimate under a constant-velocity motion model (i.e., extrapolating \mathbf{P}_{t-1} by reusing the last incremental motion), we retrieve a pose-conditioned visible subgraph $\mathcal{M}_t \subset \mathcal{M}$ to restrict matching to plausible candidates and reduce distractors. We then refine the pose by jointly considering (i) graph-level scan-to-map association and (ii) stability under weak geometric constraints:

$$\begin{aligned} \Delta\xi_t^* &= \arg \min_{\Delta\xi \in \mathbb{R}^3} \mathcal{L}_{\text{uot}} \left(\hat{\mathbf{P}}_t \exp(\Delta\xi) \mid \mathcal{S}_t, \mathcal{M}_t \right) + \mathcal{R}_{\text{deg}}(\Delta\xi), \\ \mathbf{P}_t &= \hat{\mathbf{P}}_t \exp(\Delta\xi_t^*). \end{aligned} \quad (2)$$

Here \mathcal{L}_{uot} performs scan-to-map matching via unbalanced optimal transport on graph nodes (Sec. III-C), while \mathcal{R}_{deg} stabilizes refinement in low-observability configurations through degeneracy-aware masking and delayed updates (Sec. III-D). This formulation produces a robust global pose estimate for each scan with respect to the fixed prior map, without requiring explicit chaining of relative motions.

B. Structural Registration

Given a LiDAR scan \mathbf{X}_t , our goal is to extract a compact yet reliable set of structural features for scan-to-map tracking under partial visibility and dynamic occlusions. As shown in Figure 2, we build the observation graph via a structural registration module $\mathcal{S}_t \leftarrow \text{Reg}(\mathbf{X}_t)$ that combines two complementary streams: (i) short LOAM-style sparse features and (ii) long sector-based structural lines. We fuse these streams to obtain the final point and line features used for graph construction, with improved robustness to partial visibility and dynamic occlusions.

Short sparse features from LOAM front-ends. Following common LiDAR front-ends [3], [6], we first extract a sparse set of edge-like point features and locally planar/surface cues from \mathbf{X}_t . These features are fast to compute and typically appear in large numbers, providing sufficient local constraints for iterative pose refinement. However, because they are selected from local neighborhoods, they are sensitive to transient returns caused by close-range occluders and dynamic agents (e.g., points on pedestrians or vehicles), which can dominate the curvature/smoothness statistics and reduce repeatability across frames. In low-distinctiveness segments (e.g., long straight structures) or under close-range occluders, the neighborhoods used for feature selection can be dominated by transient returns, further reducing robustness.

Long structural lines from sector-based extraction. To obtain more repeatable structural cues beyond local neighborhoods, we additionally extract long line features using a sector-based module. The scan is partitioned into angular sectors, and candidate boundary supports are detected within each sector using range discontinuities and local geometric consistency. Candidates that are consistent across neighboring sectors are aggregated into line features. Each line feature ℓ is parameterized by two endpoints and a unit direction, and represented in the graph by an anchor point (e.g., midpoint) and its direction. Compared to LOAM-style short features, long lines are typically more stable across time and viewpoint changes. However, under occlusion and limited visibility, the observed support is often truncated, which makes endpoints ambiguous and can lead to fragmented or drifting line segments—a key issue that we explicitly address in this work. These long lines may also provide weaker instantaneous constraints in degenerate layouts (e.g., many near-parallel lines).

A practical difficulty of long lines is that their utility hinges on reliable endpoints. When a boundary is partially occluded, the visible support becomes truncated and endpoints can drift with the fragment, which may cause erroneous merging of unrelated structures. We explicitly handle common occlusion patterns (illustrated in Figure 3) during sector aggregation: (a) Hidden junction cues: when corners/intersections are not directly observed, we infer a soft intersection hypothesis from stable neighboring directions and treat it as weak evidence to stabilize endpoint placement, without making hard commitments. (b) Truncation under temporary occlusion: we estimate line direction from visible inliers and update endpoints conservatively within verified visible sectors, avoiding aggressive extension beyond observed support. (c) Viewpoint-induced

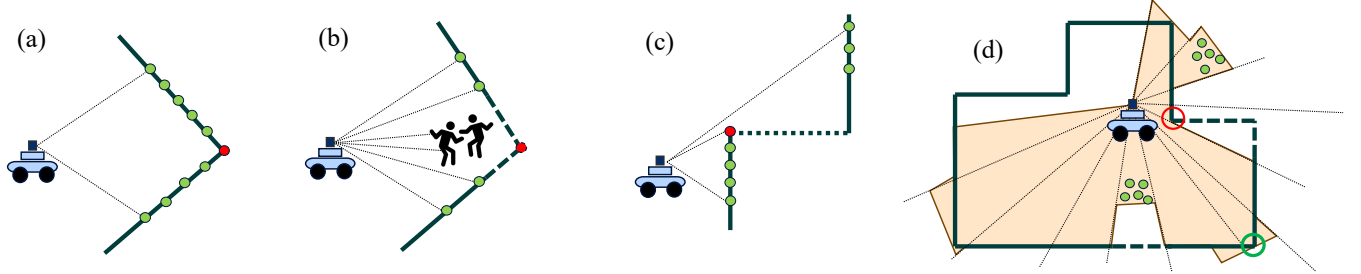


Fig. 3: Illustration of structural corner inference under different occlusion scenarios. (a) Corners/intersections are not directly observed. (b) Temporary occlusion by dynamic objects. (c) Viewpoint-induced structural missingness. (d) Sector-based reasoning parallelized across angular bins.

missing orthogonal walls: in corridor-like scenes, the scan may observe two long parallel side walls, while the orthogonal end wall is outside the field of view, yielding anisotropic constraints. Under a Manhattan-world assumption, we hypothesize a weak orthogonal line to complement the missing structure and use it as soft evidence for stabilizing estimation, without enforcing hard completion when the orthogonal surface is not directly observed. These strategies improve the repeatability of long lines under occlusion while preventing over-extension when structural endpoints are not observable.

Fusion for dynamic filtering. Dynamic objects often produce short-lived returns that break geometric continuity. To suppress such interference, we fuse the two feature streams: LOAM-style point features are validated against nearby stable line supports, retaining points that are geometrically consistent with extracted lines (and down-weighting/discardng unsupported ones); conversely, line candidates without sufficient local support are removed to avoid spurious completion. This fusion yields a filtered set of point and line features that is more robust to dynamics and partial visibility, and forms the node set of \mathcal{S}_t .

Pose-conditioned prior retrieval via LiDAR ray simulation. Given the previous estimate \mathbf{P}_{t-1} , we form a pose prediction under a constant-velocity assumption by reusing the last incremental motion:

$$\hat{\mathbf{P}}_t = \mathbf{P}_{t-1} \exp(\hat{\xi}_{t-1}), \quad \hat{\xi}_{t-1} = \log(\mathbf{P}_{t-2}^{-1} \mathbf{P}_{t-1}) \in \mathbb{R}^3, \quad (3)$$

where $\log(\cdot)$ maps an $\text{SE}(2)$ transform to its minimal 3-DoF vector representation (planar translation and yaw). We use $\hat{\mathbf{P}}_t$ to retrieve a pose-conditioned visible subgraph $\mathcal{M}_t \subset \mathcal{M}$ and initialize the subsequent scan-to-map refinement in Eq. (2). Specifically, as shown in Figure 3(d), we simulate LiDAR emission in the map frame by casting rays that follow the sensor's azimuth-elevation sampling pattern. For each ray originating at the sensor center, we query its first intersection with prior structural elements under a maximum range constraint. Only the hit elements (and their local neighborhoods) are kept to form \mathcal{M}_t . This visibility-aware retrieval (i) removes distractors outside the current view, reducing ambiguity in repetitive layouts, and (ii) significantly shrinks the candidate set, accelerating the subsequent matching while preserving local relational consistency within the visible region.

C. Unbalanced Optimal Transport for Feature Matching

Given the observation graph \mathcal{S}_t and the retrieved prior subgraph \mathcal{M}_t , correspondences are computed by a single unbalanced optimal transport (UOT) problem on graph nodes. Pairwise geometric costs score candidate feature pairs, while graph edges supply local context to reduce ambiguity in repetitive layouts. The unbalanced formulation is essential under occlusion and dynamics: extracted features can be missing or spurious, and long structures may be fragmented by viewpoint and occlusion, making strict one-to-one, mass-preserving matching unnecessarily brittle.

Formally, let $\mathcal{G}_x = (\mathcal{V}_x, \mathcal{E}_x)$ and $\mathcal{G}_y = (\mathcal{V}_y, \mathcal{E}_y)$ denote the source and target graphs. Under a candidate planar pose $\mathbf{P} \in \text{SE}(2)$, we estimate a nonnegative transport plan $\gamma \in \mathbb{R}_+^{|\mathcal{V}_x| \times |\mathcal{V}_y|}$ by

$$\gamma^*(\mathbf{P}) = \arg \min_{\gamma \geq 0} \underbrace{\langle \gamma, C(\mathbf{P}) \rangle}_{\text{geometric matching}} + \beta \underbrace{\Omega_{\text{rel}}(\gamma; \mathcal{E}_x, \mathcal{E}_y)}_{\text{context coupling}} + \rho \underbrace{D_{\text{uot}}(\gamma; \mu, \nu)}_{\text{mass relaxation}} + \varepsilon \underbrace{\mathcal{H}(\gamma)}_{\text{entropic smoothing}}, \quad (4)$$

where $\langle \gamma, C(\mathbf{P}) \rangle = \sum_{i,j} \gamma_{ij} C_{ij}(\mathbf{P})$ scores candidate pairs after transforming observation features into the map frame using \mathbf{P} , Ω_{rel} encourages locally consistent match sets through graph context, the KL-based term relaxes mass conservation so missing, spurious, or fragmented features are not forced into hard correspondences, and $\mathcal{H}(\gamma)$ provides entropic smoothing for a stable and efficient Sinkhorn-style solver.

Geometric matching term $\langle \gamma, C(\mathbf{P}) \rangle$. Nodes are of two types: point features and line features. Given a candidate planar pose $\mathbf{P} \in \text{SE}(2)$, we transform observation features into the map frame and define type-specific pairwise costs.

For point-point pairs, the cost is the Euclidean distance

$$c_{pp}(i, j; \mathbf{P}) = \|\mathbf{p}_i(\mathbf{P}) - \mathbf{p}_j\|_2, \quad (5)$$

where $\mathbf{p}_i(\mathbf{P})$ denotes the transformed location of the source point feature under \mathbf{P} .

For line-line pairs, each line feature is represented by a unit direction $\mathbf{d} \in \mathbb{S}^1$ and an anchor point $\mathbf{q} \in \mathbb{R}^2$ (e.g., midpoint), and the cost combines orientation discrepancy and anchor displacement:

$$c_{\ell\ell}(i, j; \mathbf{P}) = w_\theta \Delta\theta_{ij}^2 + w_\perp \|\mathbf{t}_{ij}^\perp\|_2 + w_\parallel \|\mathbf{t}_{ij}^\parallel\|_2, \quad (6)$$

with $\Delta\theta_{ij} = \arccos(|\mathbf{d}_i(\mathbf{P})^\top \mathbf{d}_j|)$ (invariant to sign flips), $\delta_{ij} = \mathbf{q}_i(\mathbf{P}) - \mathbf{q}_j$, $\mathbf{t}_{ij}^\parallel = (\delta_{ij}^\top \mathbf{d}_j) \mathbf{d}_j$, and $\mathbf{t}_{ij}^\perp = \delta_{ij} - \mathbf{t}_{ij}^\parallel$. Thus $c_{\ell\ell}$ jointly penalizes orientation mismatch, cross-track offset, and along-track shift.

Furthermore, we additionally allow directional cross-type association from observed point features to map line features. Specifically, for $v_i \in \mathcal{V}_x^p$ (observation) and $v_j \in \mathcal{V}_y^\ell$ (map), we define

$$c_{p\ell}(i, j) = \text{dist}(\mathbf{p}_i, \ell_j), \quad (7)$$

where $\text{dist}(\mathbf{p}, \ell)$ is the Euclidean point-to-line distance to the (infinite) supporting line of the map line feature ℓ_j (or to the finite line feature if a segment distance is used). This asymmetric channel is useful when the observation provides repeatable point evidence (e.g., corner-like returns) while the corresponding line evidence is weak, partially visible, or fragmented; it also avoids introducing ambiguous map-point hypotheses that are not reliably observable from a single scan.

Context coupling Ω_{rel} . To reduce ambiguity in repetitive layouts, we regularize the plan by preserving local relations. We use a sparse second-order coupling on source edges $(i, i') \in \mathcal{E}_x$:

$$\Omega_{\text{rel}}(\gamma) = \sum_{(i, i') \in \mathcal{E}_x} \sum_{j, j'} \gamma_{ij} \gamma_{i'j'} \psi((i, i'), (j, j')), \quad (8)$$

where ψ enforces rigid consistency:

(i) Point-point (distance consistency).

$$\psi_{pp}((i, i'), (j, j')) = \left(\|\mathbf{p}_i - \mathbf{p}_{i'}\|_2 - \|\mathbf{p}_j - \mathbf{p}_{j'}\|_2 \right)^2. \quad (9)$$

(ii) Line-line (angle consistency).

$$\begin{aligned} \psi_{\ell\ell}((i, i'), (j, j')) &= \left(\theta(\mathbf{d}_i, \mathbf{d}_{i'}) - \theta(\mathbf{d}_j, \mathbf{d}_{j'}) \right)^2, \\ \theta(\mathbf{a}, \mathbf{b}) &= \arccos(|\mathbf{a}^\top \mathbf{b}|). \end{aligned} \quad (10)$$

We apply ψ_{pp} when (i, i') and (j, j') are point pairs, and $\psi_{\ell\ell}$ when they are line pairs (otherwise $\psi = 0$). \mathcal{E}_x and \mathcal{E}_y are built by Euclidean k NN over feature representative positions.

Mass relaxation $D_{\text{uot}}(\gamma; \mu, \nu)$ and **entropic smoothing** $\mathcal{H}(\gamma)$. We adopt a KL-penalized unbalanced formulation that relaxes the marginal constraints:

$$D_{\text{uot}}(\gamma; \mu, \nu) = \text{KL}(\gamma \mathbf{1} \parallel \mu) + \text{KL}(\gamma^\top \mathbf{1} \parallel \nu), \quad (11)$$

where $\text{KL}(\mathbf{a} \parallel \mathbf{b}) = \sum_i a_i \log \frac{a_i}{b_i} - a_i + b_i$ is applied element-wise and $\mathbf{1}$ is an all-ones vector of compatible size. Unless stated otherwise, we use uniform masses $\mu = \frac{m}{|\mathcal{V}_x|} \mathbf{1}$ and $\nu = \frac{m}{|\mathcal{V}_y|} \mathbf{1}$ with a shared total mass m , while the penalty weight ρ controls how strongly the plan adheres to these masses. This relaxation allows partial matching when features are missing, spurious, or fragmented, which is common under occlusion and limited visibility. The entropic term is defined as $\mathcal{H}(\gamma) = -\sum_{i,j} \gamma_{ij} (\log \gamma_{ij} - 1)$. Together with $\varepsilon \mathcal{H}(\gamma)$, the KL-based marginal relaxation admits a stable unbalanced Sinkhorn solver, making the global assignment practical online.

Solver and sparsification. In practice, Eq. (4) is solved using a Sinkhorn-style iterative scaling algorithm with entropic smoothing, where the unbalanced KL penalties lead to relaxed marginal updates. To keep computation tractable online,

we exploit the sparsity induced by pose-conditioned visible-subgraph retrieval and k NN graph construction: candidate pairs (i, j) are restricted to a sparse neighborhood (e.g., within a gating radius or top- K nearest candidates under the geometric cost), and the context coupling Ω_{rel} is evaluated only on source edges $(i, i') \in \mathcal{E}_x$ with the corresponding sparse candidate pairs (j, j') . This yields an efficient approximate second-order coupling that retains local-context regularization while keeping both memory and runtime bounded in practice.

D. Degeneracy-Aware Delayed Optimization

Even with robust scan-to-map matching, pose refinement can become ill-conditioned when the visible structure provides weak constraints. For ground navigation, a typical case is a long straight segment (e.g., corridors or parking aisles), where most matched line features are (near-)parallel. Such configurations constrain lateral translation and yaw well, but weakly constrain translation along the dominant direction. As a result, per-frame refinement may inject association noise into the weakly constrained mode and accumulate drift. We therefore detect weak directions online and delay their correction until observability recovers.

After obtaining UOT correspondences, we form a local least-squares refinement problem in 3-DoF (planar translation and yaw) and compute the normal equations

$$\mathbf{H}_t = \mathbf{J}_t^\top \mathbf{W}_t \mathbf{J}_t, \quad \mathbf{g}_t = \mathbf{J}_t^\top \mathbf{W}_t \mathbf{r}_t, \quad (12)$$

where \mathbf{r}_t stacks residuals induced by matched features, \mathbf{J}_t is the Jacobian w.r.t. the increment $\Delta \xi_t \in \mathbb{R}^3$, and \mathbf{W}_t is a robust weight matrix. We perform an eigen-decomposition $\mathbf{H}_t = \mathbf{U}_t \text{diag}(\lambda_1, \lambda_2, \lambda_3) \mathbf{U}_t^\top$ with $\lambda_1 \geq \lambda_2 \geq \lambda_3$ and identify weakly observable modes by

$$\mathcal{D}_t = \{ k \in \{1, 2, 3\} \mid \lambda_k < \tau_\lambda \}, \quad (13)$$

where τ_λ is a degeneracy threshold (a relative criterion such as $\lambda_k / \lambda_1 < \tau_\lambda$ can also be used to reduce scale sensitivity).

Masked update in degenerate segments. If $\mathcal{D}_t \neq \emptyset$, we freeze the weak eigen-modes and update only along well-constrained directions. Specifically, we construct a mask in the eigen-basis

$$\mathbf{M}_t = \mathbf{U}_t \text{diag}(m_1, m_2, m_3) \mathbf{U}_t^\top, \quad m_k = \begin{cases} 0, & k \in \mathcal{D}_t, \\ 1, & \text{otherwise,} \end{cases} \quad (14)$$

and apply a damped solve that suppresses corrections along weak modes:

$$\Delta \xi_t = -(\mathbf{H}_t + \lambda_r (\mathbf{I} - \mathbf{M}_t))^{-1} \mathbf{g}_t \triangleq \text{SolveMasked}(\mathbf{H}_t, \mathbf{g}_t; \mathcal{D}_t), \quad (15)$$

where λ_r is a large damping coefficient. In addition, we cache instantaneous information for delayed refinement:

$$\mathcal{B}_t \leftarrow \mathcal{B}_{t-1} \cup \{(\mathbf{H}_t, \mathbf{g}_t)\}, \quad \text{if } \mathcal{D}_t \neq \emptyset. \quad (16)$$

Release delayed refinement when observability recovers. Once the configuration becomes non-degenerate ($\mathcal{D}_t = \emptyset$),

Algorithm 1: System pipeline

Input: $\mathbf{X}_t, \mathcal{M}, \mathbf{P}_{t-1}, \mathbf{P}_{t-2}, \mathcal{B}_{t-1}$
Output: $\mathbf{P}_t, \mathcal{B}_t$ (and optionally $\mathbf{T}_{t-1 \rightarrow t}$)

Motion prediction (constant velocity):
 $\hat{\xi}_{t-1} \leftarrow \log(\mathbf{P}_{t-2}^{-1} \mathbf{P}_{t-1}), \hat{\mathbf{P}}_t \leftarrow \mathbf{P}_{t-1} \exp(\hat{\xi}_{t-1})$.

Graph registration: $\mathcal{S}_t \leftarrow \text{Reg}(\mathbf{X}_t), \mathcal{M}_t \leftarrow \text{RayCast}(\mathcal{M}, \hat{\mathbf{P}}_t)$.

Matching (scan → map): $\gamma^* \leftarrow \arg \min_{\gamma \geq 0} \text{Eq. (4)}$.

Degeneracy-aware delayed update: $\mathbf{H}_t \leftarrow \mathbf{J}_t^\top \mathbf{W}_t \mathbf{J}_t, \mathbf{g}_t \leftarrow \mathbf{J}_t^\top \mathbf{W}_t \mathbf{r}_t, \mathcal{D}_t \leftarrow \text{WeakDir}(\mathbf{H}_t)$.

if $\mathcal{D}_t \neq \emptyset$ **then**

- $\mathcal{B}_t \leftarrow \mathcal{B}_{t-1} \cup \{(\mathbf{H}_t, \mathbf{g}_t)\};$
- $\Delta \xi_t \leftarrow \text{SolveMasked}(\mathbf{H}_t, \mathbf{g}_t; \mathcal{D}_t);$

else

- $\bar{\mathbf{H}}_t \leftarrow \mathbf{H}_t + \sum_{(\mathbf{H}, \cdot) \in \mathcal{B}_{t-1}} \mathbf{H};$
- $\bar{\mathbf{g}}_t \leftarrow \mathbf{g}_t + \sum_{(\cdot, \mathbf{g}) \in \mathcal{B}_{t-1}} \mathbf{g};$
- $\Delta \xi_t \leftarrow -\bar{\mathbf{H}}_t^{-1} \bar{\mathbf{g}}_t;$
- $\mathcal{B}_t \leftarrow \emptyset;$

Pose update: $\mathbf{P}_t \leftarrow \hat{\mathbf{P}}_t \exp(\Delta \xi_t);$

if need incremental output **then** $\mathbf{T}_{t-1 \rightarrow t} \leftarrow \mathbf{P}_{t-1}^{-1} \mathbf{P}_t;$

TABLE I: KITTI splits for offline map construction and pose tracking [6].

Seq.	Map construction	Pose tracking
00	0000-1000	1:1540-1650, 2:3360-3860, 3:4420-4540
02	0920-3408	1:4180-4280, 2:4549-4649
05	0000-1300	1:1301-1581, 2:2300-2650
06	0000-0833	1:0834-1100
08	0000-1306	1:1400-1850

we release the delayed refinement by aggregating buffered evidence:

$$\bar{\mathbf{H}}_t = \mathbf{H}_t + \sum_{(\mathbf{H}, \mathbf{g}) \in \mathcal{B}_{t-1}} \mathbf{H}, \quad \bar{\mathbf{g}}_t = \mathbf{g}_t + \sum_{(\mathbf{H}, \mathbf{g}) \in \mathcal{B}_{t-1}} \mathbf{g}, \quad (17)$$

and compute a full update

$$\Delta \xi_t = -\bar{\mathbf{H}}_t^{-1} \bar{\mathbf{g}}_t \triangleq \text{Solve}(\bar{\mathbf{H}}_t, \bar{\mathbf{g}}_t), \quad \mathcal{B}_t \leftarrow \emptyset. \quad (18)$$

Motion propagation. During degenerate segments, we propagate the pose using a constant-velocity prior and apply only the masked refinement increment. Specifically, we predict the pose by reusing the last motion increment:

$$\hat{\mathbf{P}}_t \leftarrow \mathbf{P}_{t-1} \exp(\hat{\xi}_{t-1}), \quad \hat{\xi}_{t-1} = \log(\mathbf{P}_{t-2}^{-1} \mathbf{P}_{t-1}), \quad (19)$$

and update the estimate by

$$\mathbf{P}_t \leftarrow \hat{\mathbf{P}}_t \exp(\Delta \xi_t), \quad (20)$$

where $\Delta \xi_t$ is obtained from the masked solve in Eq. (15).

The system pipeline is summarized in Algorithm 1.

IV. EXPERIMENTS

We evaluate Graph-Loc in three complementary settings that stress different aspects of map-based pose tracking. Across all experiments, we use polygon-outline priors vectorized from occupancy/grid-style maps and perform no contour splitting.

This choice allows us to evaluate whether robust association can be achieved with an unsplit, compact prior, rather than improving matchability by inflating the map through offline contour segmentation (as commonly adopted in polygon-outline pipelines such as ERPoT [6]). By keeping outlines unsplit, we preserve the compactness of the onboard prior and isolate the effectiveness of graph-based matching and degeneracy-aware optimization.

Public benchmarks assess scalability and the accuracy-compactness trade-off in large scenes. Controlled simulation and indoor real-world experiments systematically vary the level of dynamics to analyze robustness under sustained occlusion and low observability. In addition, we include an outdoor real-world experiment in a parking-lot environment to evaluate long-range pose tracking under gradual scene changes, where static priors inevitably deviate from online observations due to temporary obstacles and scene reconfiguration. For indoor scenarios, we further report results with heterogeneous compact priors (Gazebo models in simulation and CAD layouts in real-world deployment) to demonstrate that Graph-Loc is not tied to a specific map origin and can leverage structural layouts available in practice.

A. Public Large-Scale Benchmarks

We first evaluate on two public large-scale datasets, KITTI and ERPoT, to assess scalability and outdoor localization accuracy. For each dataset, we follow the standard prior-map evaluation protocol: an offline prior is built from a dedicated mapping segment, and localization is performed on disjoint tracking segments that overlap in route. All priors are constructed offline and kept fixed during localization.

KITTI. We evaluate on KITTI sequences 00, 02, 05, 06, and 08 following the split protocol in ERPoT [6]; the exact frame ranges for map construction and pose tracking are summarized in Table I. Table II highlights the compactness advantage of structural priors: even after voxel filtering, point-cloud priors typically require tens to hundreds of MB, whereas polygon-outline priors are sub-MB. Within the polygon setting, our priors are generated from the same outline source but without contour splitting, leading to consistently smaller maps across all evaluated sequences (about 10-13% reduction) while avoiding additional offline processing. Despite using these more compact priors, our method remains competitive in accuracy. Compared with all methods, we achieve lower ATE on most tracking segments and obtain the best overall average across all evaluated splits, while keeping the map prior strictly smaller. Representative trajectories are shown in Figure 4(a)-(e). Overall, the KITTI results indicate that reliable large-scale localization does not require contour splitting when association is solved globally.

ERPoT dataset. We further evaluate on the ERPoT dataset using the official mapping/tracking splits [6]. Since the data package for sequence 01-3 is corrupted, we report results on 01-1, 01-2, and 02-1 only. Table III summarizes the quantitative results and Figure 4(f)-(g) visualizes representative trajectories. ERPoT improves matchability by offline contour segmentation that splits long outlines into shorter

TABLE II: Pose tracking results on KITTI dataset.

Sequence	Metric	ALOAM_MCL	FLOAM_MCL	KISS_MCL	HDL_LOC	ERPoT	Ours
KITTI00-1	Prior Map Size (MB)	56.44	56.44	56.44	56.44	<u>0.28</u>	0.25
	ATE [cm]	Max	92.85	136.08	74.88	361.09	<u>47.96</u> 22.02
		Mean	58.44	61.08	49.18	24.95	<u>13.14</u> 9.36
		RMSE	63.70	64.49	51.27	60.52	<u>16.33</u> 10.87
KITTI00-2	Prior Map Size (MB)	56.44	56.44	56.44	56.44	<u>0.28</u>	0.25
	ATE [cm]	Max	158.69	138.17	208.34	149.60	<u>23.66</u> 34.01
		Mean	40.92	49.73	62.20	7.72	<u>8.36</u> 9.61
		RMSE	47.96	58.74	81.73	11.32	9.53 <u>11.27</u>
KITTI00-3	Prior Map Size (MB)	56.44	56.44	56.44	56.44	<u>0.28</u>	0.25
	ATE [cm]	Max	186.50	170.32	265.02	48.52	<u>34.46</u> 26.24
		Mean	114.40	113.97	131.44	<u>8.83</u>	12.88 7.73
		RMSE	125.01	123.72	152.89	<u>10.79</u>	16.64 9.58
KITTI02-1	Prior Map Size (MB)	110.47	110.47	110.47	110.47	<u>0.85</u>	0.74
	ATE [cm]	Max	130.04	130.24	170.96	X	<u>33.13</u> 34.58
		Mean	74.96	69.36	84.73	X	<u>11.58</u> 12.22
		RMSE	76.71	73.32	90.04	X	<u>13.39</u> 15.49
KITTI02-2	Prior Map Size (MB)	110.47	110.47	110.47	110.47	<u>0.85</u>	0.74
	ATE [cm]	Max	X	X	X	181.80	<u>83.44</u> 40.45
		Mean	X	X	X	140.22	<u>18.70</u> 14.13
		RMSE	X	X	X	142.50	<u>22.10</u> 15.92
KITTI05-1	Prior Map Size (MB)	70.93	70.93	70.93	70.93	0.36	0.32
	ATE [cm]	Max	63.42	127.64	96.40	149.28	<u>25.46</u> 24.34
		Mean	32.76	40.94	48.07	<u>8.12</u>	7.94 8.94
		RMSE	35.56	50.25	53.91	19.02	9.01 <u>10.29</u>
KITTI05-2	Prior Map Size (MB)	70.93	70.93	70.93	70.93	<u>0.36</u>	0.32
	ATE [cm]	Max	101.97	216.58	117.28	103.83	<u>26.84</u> 23.07
		Mean	43.56	65.23	51.24	10.68	<u>10.14</u> 9.25
		RMSE	50.42	85.12	60.81	13.14	<u>11.14</u> 10.39
KITTI06-1	Prior Map Size (MB)	56.90	56.90	56.90	56.90	<u>0.27</u>	0.24
	ATE [cm]	Max	X	X	547.68	X	<u>28.78</u> 17.90
		Mean	X	X	243.60	X	<u>7.25</u> 6.17
		RMSE	X	X	276.71	X	<u>8.08</u> 7.30
KITTI08-1	Prior Map Size (MB)	133.01	133.01	133.01	133.01	<u>0.59</u>	0.53
	ATE [cm]	Max	X	X	X	<u>61.26</u>	78.01 46.25
		Mean	X	X	X	24.60	16.10 <u>18.71</u>
		RMSE	X	X	X	28.24	<u>22.47</u> 21.63
Avg.	ATE [cm]	Max	X	X	X	X	<u>41.65</u> 27.32
		Mean	X	X	X	X	<u>11.90</u> 10.46
		RMSE	X	X	X	X	<u>13.81</u> 11.94

primitives, whereas we keep the outlines unsplit and instead rely on global unbalanced-OT graph matching together with degeneracy-aware refinement. Under the same prior source and split protocol, removing contour splitting consistently reduces the map prior size across sequences (about 10-15%) while preserving robust tracking behavior.

In terms of accuracy, our method achieves a lower average ATE than ERPoT across the evaluated sequences. We observe clear improvements on 01-1 and 01-2. On 02-1, our error is slightly higher than ERPoT, but the estimated trajectory remains stable and well aligned throughout the sequence, with no divergence or tracking failures. Overall, these results support that robust global association can reduce reliance on contour splitting: compact polygon-outline priors can remain matchable and achieve competitive (and on average improved) localization accuracy under the standard ERPoT evaluation

protocol.

B. Controlled Degeneracy and Occlusion Study

We conduct a controlled study in the CMU-EXPLORATION environment [13] to evaluate pose tracking with compact priors under weak observability and occlusion. This environment contains long and repeated structures that often yield low-distinctiveness measurements for scan-to-map alignment, and a social-force-based pedestrian simulator enables systematic control of dynamic occlusions. Following the same protocol as the public benchmarks, we build a fixed prior map offline and evaluate localization on three tracking sequences that are disjoint from the mapping run. The sequences replay the same route while varying only the number of pedestrians (0, 5, and 20), corresponding to static, mild-occlusion, and heavy-occlusion conditions.

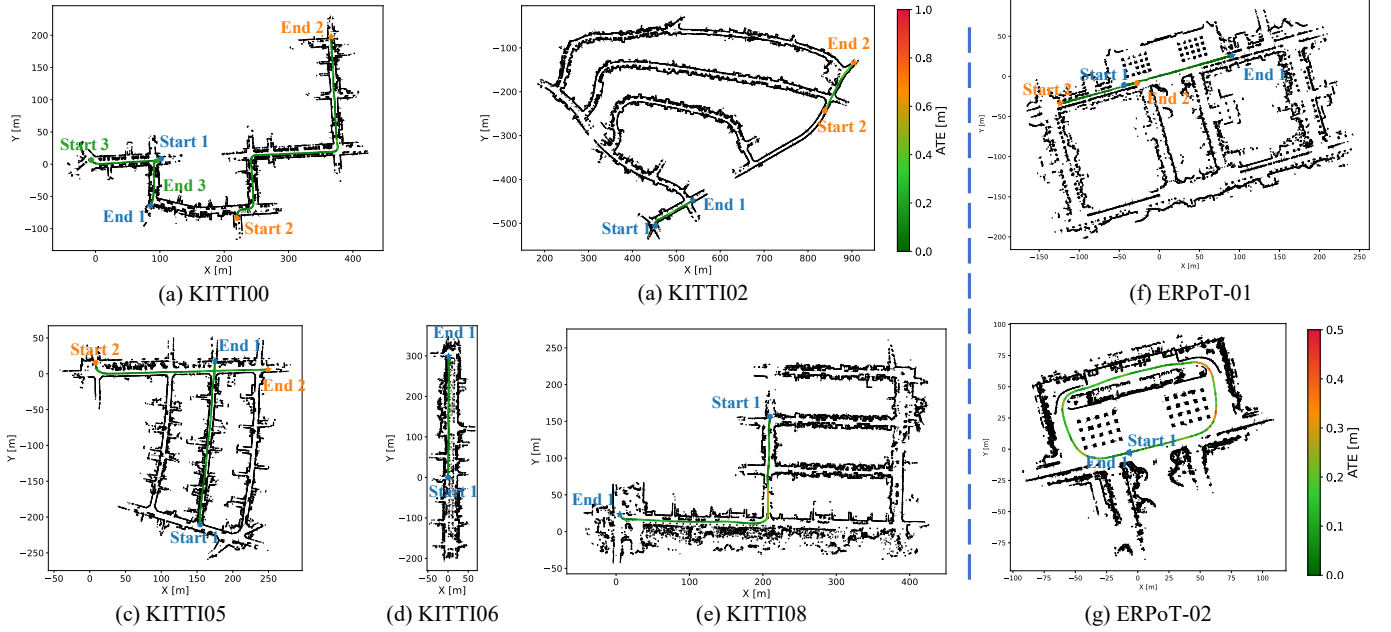


Fig. 4: Qualitative results of our method on KITTI and ERPoT dataset.

TABLE III: Pose tracking results on the ERPoT dataset.

Sequence	Metric	ALOAM_MCL	FLOAM_MCL	KISS_MCL	HDL_LOC	ERPoT	Ours
ERPoT-01-1	Prior Map Size (MB)	111.91	111.91	111.91	111.91	<u>0.98</u>	0.87
	Max	53.49	109.57	87.40	✗	<u>22.26</u>	<u>30.42</u>
	Mean	24.30	33.12	27.74	✗	<u>9.48</u>	5.39
	RMSE	26.08	40.95	32.71	✗	<u>10.24</u>	6.57
ERPoT-01-2	Prior Map Size (MB)	111.91	111.91	111.91	111.91	<u>0.98</u>	0.87
	Max	27.28	42.27	37.07	21.03	<u>28.83</u>	16.29
	Mean	13.14	14.44	22.11	14.05	<u>6.97</u>	4.82
	RMSE	14.03	15.35	23.59	14.33	<u>7.99</u>	5.47
ERPoT-02-1	Prior Map Size (MB)	32.92	32.92	32.92	32.92	<u>0.65</u>	0.56
	Max	102.32	53.06	92.98	50.67	29.62	<u>32.89</u>
	Mean	23.09	16.47	20.29	4.81	<u>6.33</u>	8.79
	RMSE	30.57	20.15	26.28	6.18	<u>7.55</u>	10.61
Avg.	Max	61.03	68.30	72.48	✗	<u>26.90</u>	26.53
	Mean	20.18	21.34	23.38	✗	<u>7.59</u>	6.33
	RMSE	23.56	25.48	27.53	✗	<u>8.59</u>	7.55

Priors and baselines. We report results under two compact prior sources: (i) a structural layout prior distilled from the Gazebo model, and (ii) polygon outlines vectorized from occupancy/grid-style maps. For the polygon prior, our method keeps the outlines unsplit to preserve compactness. In this degeneracy-dominant setting, the original ERPoT polygon pipeline is not directly runnable. To include ERPoT as a reference, we additionally apply a length-based splitting rule (beyond its default segmentation) to break long polygons into shorter primitives. With this modification, ERPoT becomes trackable only in the no-pedestrian condition, while requiring a substantially larger polygon map (about $6\times$ compared to the unsplit polygon prior); under pedestrian occlusions, it remains unstable and does not provide reliable tracking.

Results and analysis. Table IV reports quantitative results and Figure 5 visualizes representative trajectories and map

constructions. With the Gazebo-derived structural prior, the resulting map provides clean and stable constraints, yielding reliable tracking in static and mild-occlusion conditions. With the unsplit polygon-outline prior, our method maintains stable trajectory alignment as occlusion increases, indicating that compact occupancy-derived priors can remain effective without contour splitting when association is solved globally and pose updates are stabilized by degeneracy-aware refinement.

Overall, this controlled study complements the outdoor benchmarks by explicitly varying occlusion density under low-observability structure, and further demonstrates that the proposed framework supports heterogeneous compact priors (occupancy-derived outlines and layout-based priors) with consistent robustness.

TABLE IV: Pose tracking results on CMU-EXPLORATION.

Map Type	Method	Prior Map Size (KB) ↓	0 People (ATE [cm])			5 People (ATE [cm])			20 People (ATE [cm])		
			Max ↓	Mean ↓	RMSE ↓	Max ↓	Mean ↓	RMSE ↓	Max ↓	Mean ↓	RMSE ↓
Point Cloud	HDL_LOC	3027.21	97.12	8.31	9.81	97.30	8.40	9.66	✗	✗	✗
	ALOAM_MCL	3027.21	<u>16.69</u>	9.22	9.53	<u>16.90</u>	9.26	<u>9.57</u>	26.87	<u>9.90</u>	<u>11.05</u>
Gazebo Model	PS_LOC	4.5	40.12	15.32	17.12	45.21	25.38	27.12	✗	✗	✗
	Ours	4.5	14.78	<u>6.40</u>	7.34	15.88	6.41	7.40	✗	✗	✗
Polygon Map	ERPoT	8.0	✗	✗	✗	✗	✗	✗	✗	✗	✗
	ERPoT*	43	38.34	8.04	11.98	✗	✗	✗	✗	✗	✗
	Ours	7.2	25.50	6.12	<u>8.09</u>	29.21	<u>7.94</u>	9.86	<u>54.13</u>	9.05	10.64

TABLE V: Pose tracking results on real degeneracy and occlusion.

Map Type	Method	Prior Map Size (KB) ↓	0 People (ATE [cm])			5 People (ATE [cm])		
			Max ↓	Mean ↓	RMSE ↓	Max ↓	Mean ↓	RMSE ↓
Point Cloud	HDL_LOC	2682.88	47.64	22.40	25.06	50.20	22.83	25.33
	ALOAM_MCL	5365.76	43.68	19.54	21.82	<u>50.07</u>	20.40	22.50
CAD	PS_LOC	24.8	50.33	20.12	22.23	52.67	22.21	23.58
	Ours	24.8	30.91	11.47	13.76	58.98	<u>14.04</u>	<u>17.80</u>
Polygon Map	ERPoT	184	61.26	15.20	18.08	✗	✗	✗
	Ours	154	<u>35.21</u>	<u>12.80</u>	<u>15.29</u>	30.28	13.80	15.00

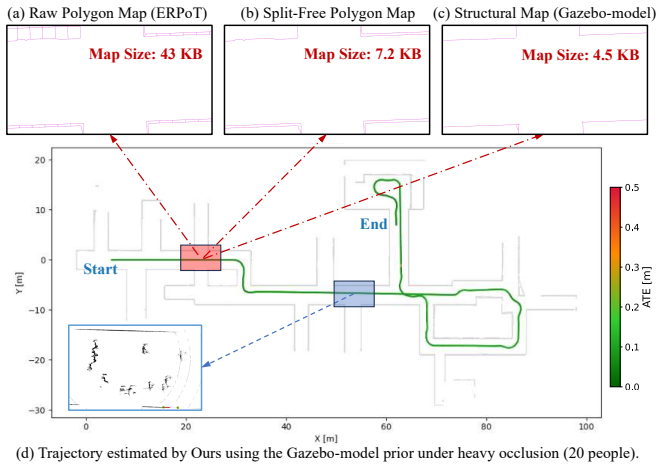


Fig. 5: Qualitative results of our method on CMU-EXPLORATION (20 people).

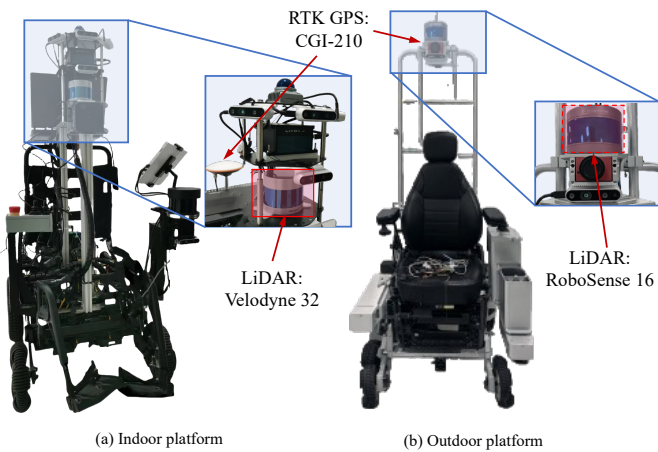


Fig. 6: Our data-collection platforms.

C. Real-World Experiments

We conduct real-world experiments to validate deployable pose tracking with compact priors under two practical factors: (i) weak observability with sustained short-range occlusions, and (ii) long-range tracking under gradual scene changes. Figure 6 shows the two data-collection platforms. The first setup targets ground navigation in a corridor-like route using a Velodyne 32-beam LiDAR, where observations are often dominated by repeated straight structures and frequently interrupted by nearby occluders. The second setup targets a parking-lot traversal using a RoboSense 16-beam LiDAR, where the map prior can be imperfect due to parked vehicles, temporary obstacles, and local layout variations across days. For evaluation, outdoor ground truth is provided by RTK-GPS, while indoor reference trajectories are produced by an offline LIVO pipeline with dynamic filtering and loop-closure optimization.

Degeneracy and occlusion. Two sequences are collected in the same site: a mostly static run and a run with 5 pedestrians repeatedly crossing near the platform. The prior map is built from an independent mapping session recorded on a different day. As reported in Table V, the proposed method achieves the best overall accuracy across both sequences while running online in real time. With the CAD prior in the static run, the clean layout cues enable reliable scan-to-map alignment, and the proposed global graph matching improves accuracy over the CAD-based baseline. With pedestrian interference, a non-negligible portion of measurements becomes missing or corrupted; nevertheless, the proposed method remains stable and consistently outperforms both point-cloud-prior and polygon-prior baselines. Figure 7 visualizes the trajectory on the 5-people run with the CAD prior, illustrating accurate real-time tracking under sustained occlusions.

Tracking under environment changes. We further evaluate long-range tracking on a parking-lot sequence with noticeable environment changes across time. Table VI and Figure 8 report results using point-cloud priors and polygon-outline

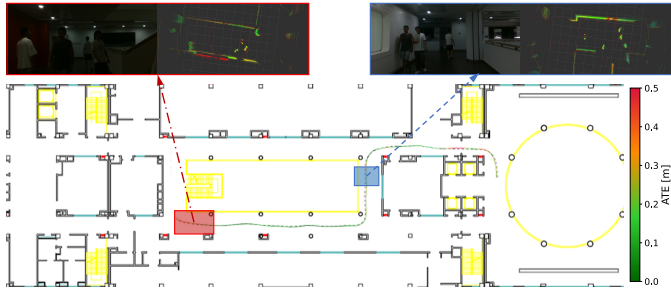


Fig. 7: Trajectory estimated by our method using the CAD prior under pedestrian occlusion (5 people).

TABLE VI: Pose tracking results on environment changes.

Method	Prior Map Size (MB) ↓	ATE [cm]		
		Max ↓	Mean ↓	RMSE ↓
HDL_LOC	3.0	65.49	11.10	12.83
ALOAM_MCL	3.0	✗	✗	✗
ERPoT	0.15	110.6	27.79	33.69
Ours	0.13	46.63	5.18	7.42

priors. Our method achieves the best accuracy among all compared approaches, obtaining the lowest ATE while using a compact polygon-outline prior. In particular, compared with the split-based polygon pipeline ERPoT, our method substantially reduces the trajectory error and remains stable under partial visibility and prior mismatch caused by parked vehicles and temporary obstacles. Compared with the point-cloud baseline HDL_LOC, our method also yields lower ATE across all metrics, while requiring a much smaller prior map. Overall, the outdoor results indicate that compact polygon priors can support accurate and stable long-range localization under gradual scene changes, without contour splitting or map inflation.

D. Ablation Study

Table VII reports an ablation study on KITTI, ERPoT, and the controlled indoor simulation. We ablate three key components: dynamic filtering (D.F.), unbalanced optimal transport matching (O.T.), and degeneracy-aware delayed optimization (D.T.).

Across datasets, the **unbalanced optimal transport** module is the most critical. Removing it causes the largest and most consistent degradation on both KITTI and ERPoT, even though these benchmarks are static or near-static. In the ablated setting without unbalanced optimal transport, correspondences are computed using the same nearest-neighbor association scheme as ERPoT [6], i.e., each feature selects its closest candidate under the current pose estimate and the pose is refined by iterative re-alignment. The clear performance gap indicates that local nearest-neighbor decisions are particularly brittle in repetitive or weakly distinctive structures, whereas the global transport plan provides substantially more reliable association signals for pose tracking.

The **degeneracy-aware delayed optimization** becomes especially important in structurally degenerate segments. While robust matching provides reliable correspondences, the pose update can still be ill-conditioned when the visible structure

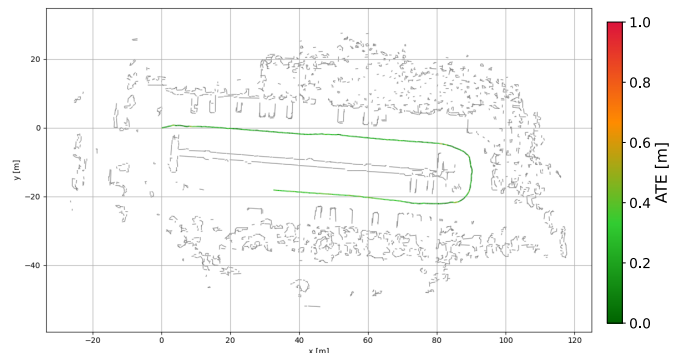


Fig. 8: Trajectory estimated by our method using the Polygon map under environment changes.

TABLE VII: Ablation study of different components on KITTI, ERPoT and Indoor simulation datasets (RMSE [cm]). D.F. denotes dynamic feature filtering, O.T. denotes correspondence estimation via unbalanced optimal-transport graph matching, and D.T. denotes degeneracy-aware delayed optimization.

Sequence	w.o. D.F.	w.o. O.T.	w.o. D.T.	Full
KITTI00-1	11.2	21.4	13.3	10.9
KITTI00-2	12.1	26.4	14.1	11.3
KITTI00-3	10.7	23.4	14.8	9.6
KITTI02-1	17.2	17.4	16.3	15.5
KITTI02-2	17.6	16.1	20.5	15.9
KITTI05-1	12.3	13.4	11.6	10.3
KITTI05-2	14.1	16.1	10.9	10.4
KITTI06-1	10.2	✗	8.0	7.3
KITTI08-1	22.1	25.7	21.6	21.3
ERPoT-01-1	6.8	8.9	8.0	6.6
ERPoT-01-2	6.7	8.6	5.6	5.5
ERPoT-02-1	13.2	13.8	17.3	10.6
CMU_0	8.8	12.0	25.7	8.1
CMU_5	11.3	✗	28.0	9.9
CMU_20	17.3	✗	30.9	10.6

offers weak constraints (e.g., long corridors or dominant parallel boundaries). This effect is most evident in the controlled indoor simulation: disabling the delayed optimization leads to a pronounced performance drop, and the gap grows as occlusion increases (CMU_5 and CMU_20). By damping updates along weakly observable directions and postponing aggressive corrections until sufficient constraints accumulate, the delayed optimization stabilizes tracking under low observability.

The **dynamic filtering** module mainly improves robustness under dynamics. Since KITTI, ERPoT, and CMU_0 are static or quasi-static, removing dynamic filtering yields a comparatively smaller change there. Its contribution is expected to be more pronounced when dynamic occluders and clutter introduce transient returns and fragment measurements, where filtering suppresses unreliable features and reduces the burden on subsequent matching and optimization.

Overall, the ablation supports a clear division of roles: optimal transport matching provides the core robust association capability, dynamic filter stabilizes optimization under low observability, and delayed optimization complements them

TABLE VIII: Runtime comparison.

Method	Max [ms]	Mean [ms]	Min [ms]	SD [ms]
ERPoT	162.00	100.17	51.00	21.60
Our Method (CPU)	394.00	63.91	1.00	45.50
Our Method (GPU)	62.00	24.56	6.00	6.86

when dynamics dominate the measurements.

E. Runtime

As shown in Table VIII, we report runtime on the CMU-EXPLORATION benchmark by running 10 independent trials and measuring the per-scan processing time for each method. All methods are run a PC with Intel i5 14600kf and RTX 5060ti. Overall, our GPU implementation achieves the lowest mean latency and a substantially tighter worst-case bound than ERPoT, while the CPU implementation remains competitive in mean time but exhibits a larger variance. A key reason is that the optimal transport solver is particularly amenable to GPU acceleration. Its Sinkhorn-style iterations are dominated by element-wise operations and matrix-vector/matrix-matrix primitives, which map efficiently to GPU kernels. In contrast, ERPoT relies on thresholded association followed by heuristic iterative refinement and pruning. By solving correspondences globally and typically converging to a stable transport plan in a small, fixed number of iterations, the proposed matching reaches stable associations faster in practice, leading to the runtime advantage.

V. CONCLUSION

We presented Graph-Loc, a graph-based LiDAR pose tracking framework that localizes against compact structural priors represented as lightweight point-line graphs. While our primary focus is on split-free polygon outlines vectorized from occupancy/grid-style maps, Graph-Loc also supports heterogeneous compact priors commonly available in practice, including CAD/model/floor-plan layouts in indoor scenarios. Scan-to-map association is solved globally via unbalanced optimal transport with graph-context regularization, reducing the reliance on offline contour segmentation that inflates the map to improve matchability. The unbalanced formulation relaxes strict mass conservation, making matching tolerant to missing, spurious, and fragmented observations under occlusion and partial visibility. To stabilize pose refinement in low-observability segments (e.g., corridor-like layouts dominated by parallel structures), we further introduced a degeneracy-aware delayed optimization strategy that detects weakly constrained motion directions, accumulates reliable constraints, and releases full updates once observability recovers. Experiments on KITTI and ERPoT show that split-free polygon priors can achieve competitive tracking accuracy while consistently reducing prior size compared to split-based polygon pipelines. Controlled simulation and real-world deployments further validate robustness under sustained occlusion and gradual scene changes, and additional indoor results with heterogeneous priors demonstrate that the proposed matching and optimization are not tied to a specific map origin.

REFERENCES

- [1] Y. Lu, H. Ma, E. Smart, and H. Yu, “Real-time performance-focused localization techniques for autonomous vehicle: A review,” *IEEE Transactions on Intelligent Transportation Systems*, vol. 23, no. 7, pp. 6082–6100, 2021.
- [2] H. Yin, X. Xu, S. Lu, X. Chen, R. Xiong, S. Shen, C. Stachniss, and Y. Wang, “A survey on global lidar localization: Challenges, advances and open problems,” *International Journal of Computer Vision*, vol. 132, no. 8, pp. 3139–3171, 2024.
- [3] J. Zhang, S. Singh *et al.*, “Loam: Lidar odometry and mapping in real-time,” in *Robotics: Science and systems*, vol. 2, no. 9. Berkeley, CA, 2014, pp. 1–9.
- [4] I. Vizzo, T. Guadagnino, B. Mersch, L. Wiesmann, J. Behley, and C. Stachniss, “Kiss-icp: In defense of point-to-point icp-simple, accurate, and robust registration if done the right way,” *IEEE Robotics and Automation Letters*, vol. 8, no. 2, pp. 1029–1036, 2023.
- [5] H. Wang, C. Wang, C.-L. Chen, and L. Xie, “F-loam: Fast lidar odometry and mapping,” in *2021 IEEE/RSJ International Conference on Intelligent Robots and Systems (IROS)*. IEEE, 2021, pp. 4390–4396.
- [6] H. Gao, Q. Qiu, H. Liu, D. Liang, C. Wang, and X. Zhang, “Erpot: Effective and reliable pose tracking for mobile robots using lightweight polygon maps,” *IEEE Transactions on Robotics*, 2025.
- [7] H. Gao, X. Zhang, J. Wen, J. Yuan, and Y. Fang, “Autonomous indoor exploration via polygon map construction and graph-based slam using directional endpoint features,” *IEEE Transactions on Automation Science and Engineering*, vol. 16, no. 4, pp. 1531–1542, 2018.
- [8] H. Cheng, H. Chen, and Y. Liu, “Topological indoor localization and navigation for autonomous mobile robot,” *IEEE Transactions on Automation Science and Engineering*, vol. 12, no. 2, pp. 729–738, 2014.
- [9] B. Wijaya, K. Jiang, M. Yang, T. Wen, Y. Wang, X. Tang, Z. Fu, T. Zhou, and D. Yang, “High definition map mapping and update: A general overview and future directions,” *arXiv preprint arXiv:2409.09726*, 2024.
- [10] K. Ebadi, M. Palieri, S. Wood, C. Padgett, and A.-a. Aghamohammadi, “Dare-slam: Degeneracy-aware and resilient loop closing in perceptually-degraded environments,” *Journal of Intelligent & Robotic Systems*, vol. 102, no. 1, p. 2, 2021.
- [11] F. Boniardi, T. Caselitz, R. Kümmel, and W. Burgard, “A pose graph-based localization system for long-term navigation in cad floor plans,” *Robotics and Autonomous Systems*, vol. 112, pp. 84–97, 2019.
- [12] A. Geiger, P. Lenz, C. Stiller, and R. Urtasun, “Vision meets robotics: The kitti dataset,” *The International Journal of Robotics Research*, vol. 32, no. 11, pp. 1231–1237, 2013.
- [13] C. Cao, H. Zhu, Z. Ren, H. Choset, and J. Zhang, “Representation granularity enables time-efficient autonomous exploration in large, complex worlds,” *Science Robotics*, vol. 8, no. 80, p. eadf0970, 2023.
- [14] K. Koide, J. Miura, and E. Menegatti, “A portable three-dimensional lidar-based system for long-term and wide-area people behavior measurement,” *International Journal of Advanced Robotic Systems*, vol. 16, no. 2, p. 1729881419841532, 2019.
- [15] L. Tang, Y. Wang, X. Ding, H. Yin, R. Xiong, and S. Huang, “Topological local-metric framework for mobile robots navigation: a long term perspective,” *Autonomous Robots*, vol. 43, pp. 197–211, 2019.
- [16] Y. Liu, J. Tao, B. He, Y. Zhang, and W. Dai, “Error analysis-based map compression for efficient 3-d lidar localization,” *IEEE Transactions on Industrial Electronics*, vol. 70, no. 10, pp. 10 323–10 332, 2022.
- [17] T. Shan, B. Englot, D. Meyers, W. Wang, C. Ratti, and D. Rus, “Lio-sam: Tightly-coupled lidar inertial odometry via smoothing and mapping,” in *2020 IEEE/RSJ international conference on intelligent robots and systems (IROS)*. IEEE, 2020, pp. 5135–5142.
- [18] X. Chen, I. Vizzo, T. Läbe, J. Behley, and C. Stachniss, “Range image-based lidar localization for autonomous vehicles,” in *2021 IEEE International Conference on Robotics and Automation (ICRA)*. IEEE, 2021, pp. 5802–5808.
- [19] F. Boniardi, T. Caselitz, R. Kümmel, and W. Burgard, “Robust lidar-based localization in architectural floor plans,” in *2017 IEEE/RSJ International Conference on Intelligent Robots and Systems (IROS)*. IEEE, 2017, pp. 3318–3324.
- [20] J. Luo, Q. Ye, S. Zhang, and Z. Yang, “Indoor mapping using low-cost mls point clouds and architectural skeleton constraints,” *Automation in Construction*, vol. 150, p. 104837, 2023.
- [21] D. Xu, J. Liu, J. Hyppä, Y. Liang, and W. Tao, “A heterogeneous 3d map-based place recognition solution using virtual lidar and a polar grid height coding image descriptor,” *ISPRS Journal of Photogrammetry and Remote Sensing*, vol. 183, pp. 1–18, 2022.

- [22] Y. Xie, W. Zhao, J. Wang, J. Wang, and W. Chen, “Precise lidar slam in structured scene using finite plane and prior constraint,” in *2022 IEEE International Conference on Robotics and Biomimetics (ROBIO)*, 2022, pp. 584–589.
- [23] P. J. Besl and N. D. McKay, “Method for registration of 3-d shapes,” in *Sensor fusion IV: control paradigms and data structures*, vol. 1611. Spie, 1992, pp. 586–606.
- [24] J. Zhang, Y. Yao, and B. Deng, “Fast and robust iterative closest point,” *IEEE Transactions on Pattern Analysis and Machine Intelligence*, vol. 44, no. 7, pp. 3450–3466, 2021.
- [25] P. Biber and W. Straßer, “The normal distributions transform: A new approach to laser scan matching,” in *Proceedings 2003 IEEE/RSJ International Conference on Intelligent Robots and Systems (IROS 2003)(Cat. No. 03CH37453)*, vol. 3. IEEE, 2003, pp. 2743–2748.
- [26] A. Shafiezadeh, N. P. Bhatt, and E. Hashemi, “Lidar-based navigation using normal distributions transform filter,” in *2024 IEEE 27th International Conference on Intelligent Transportation Systems (ITSC)*. IEEE, 2024, pp. 4046–4051.
- [27] M. Cuturi, “Sinkhorn distances: Lightspeed computation of optimal transport,” *Advances in neural information processing systems*, vol. 26, 2013.
- [28] R. Li, W. Zhao, T. Deng, Y. Wang, and J. Wang, “Ps-loc: Robust lidar localization with prior structural reference,” in *2024 IEEE/RSJ International Conference on Intelligent Robots and Systems (IROS)*. IEEE, 2024, pp. 12 234–12 239.
- [29] R. Yunus, Y. Li, and F. Tombari, “Manhattanslam: Robust planar tracking and mapping leveraging mixture of manhattan frames,” in *2021 IEEE International Conference on Robotics and Automation (ICRA)*. IEEE, 2021, pp. 6687–6693.
- [30] K. Joo, T.-H. Oh, F. Rameau, J.-C. Bazin, and I. S. Kweon, “Linear rgb-d slam for atlanta world,” in *2020 IEEE International Conference on Robotics and Automation (ICRA)*. IEEE, 2020, pp. 1077–1083.
- [31] H. Li, J. Zhao, J.-C. Bazin, P. Kim, K. Joo, Z. Zhao, and Y.-H. Liu, “Hong kong world: Leveraging structural regularity for line-based slam,” *IEEE Transactions on Pattern Analysis and Machine Intelligence*, vol. 45, no. 11, pp. 13 035–13 053, 2023.
- [32] Y. Gong, F. Sun, J. Yuan, W. Zhu, and Q. Sun, “A two-level framework for place recognition with 3d lidar based on spatial relation graph,” *Pattern Recognition*, vol. 120, p. 108171, 2021.
- [33] M. Shaheer, J. A. Millan-Romera, H. Bavle, J. L. Sanchez-Lopez, J. Civera, and H. Voos, “Graph-based global robot localization informing situational graphs with architectural graphs,” in *2023 IEEE/RSJ International Conference on Intelligent Robots and Systems (IROS)*. IEEE, 2023, pp. 9155–9162.
- [34] Y. Zhang, F. Tang, and Y. Wu, “Cornevins: Accurate localization and layout mapping for structural environments leveraging hierarchical geometric representations,” *IEEE Transactions on Robotics*, 2025.